RESEARCH ARTICLE

Novel End-Winding Hybrid Flux Machine

BOWEN SHI[1,2], XIAOYAN HUANG [1], (Member, IEEE), JING LI[3], (Senior Member, IEEE), HE ZHANG [3], (Senior Member, IEEE), HAN ZHAO[2,4], XIAOCHEN ZHANG [3,4], (Member, IEEE), FENGYU ZHANG [5], (Member, IEEE), AND CHRIS GERADA [5], (Senior Member, IEEE)

[1]College of Electrical Engineering, Zhejiang University, Hangzhou 310058, China
[2]Nottingham Electrification Center, University of Nottingham Ningbo China, Ningbo 315100, China
[3]Key Laboratory of More Electric Aircraft Technology of Zhejiang Province, University of Nottingham Ningbo China, Ningbo 315100, China
[4]Advanced Electric Drive Centre, Yongjiang Laboratory, Ningbo 315202, China
[5]Power Electronics, Machines and Control Group, University of Nottingham, NG7 2RD Nottingham, U.K.

Corresponding author: Jing Li (Jing.Li@nottingham.edu.cn)

ABSTRACT This paper presents a novel motor topology, called the End-Winding Flux Machine (EWM), which explores the potential function of end-windings in rotating electric machines. By introducing an axial-radial flux stator into the end-windings, a hybrid flux machine known as the End-Winding Hybrid Flux Machine (EHFM) is created, establishing an additional radial-axial flux circuit alongside the conventional radial-flux machine. The machine characteristics of the EHFM are validated through analytical calculations and transient 3-D finite-element method (FEM). Experimental investigations are conducted on a prototype EHFM, and the tested data is compared with FEM results. The EHFM exhibits enhanced torque performance compared to the benchmark motor within the same input current and armature winding specifications. These findings demonstrate the effectiveness of the proposed design and its potential for improving end-wingding utilization and torque performance in electric machines.

INDEX TERMS End-winding, axial-radial flux, hybrid flux machine, torque performance.

I. INTRODUCTION

Conventional radial flux machines face significant challenges in terms of performance improvement and in reducing issues related to end-winding. One of the main concerns is that extending the end-winding can lead to additional copper losses, flux leakage and have a negative impact on motor performance, particularly in terms of volume size. In contrast to the winding situated within the motor slots, the thermal management and heat distribution challenges associated with end-winding have consistently constituted a substantial impediment to advancing the power density of electric motors. These issues can further hinder the overall performance of the machine [1], [2], [3], [4]. To address these challenges, several papers have explored or proposed different typologies of electric machines. These approaches aim to enhance the flux performance or leverage the side effects of the end-winding in order to achieve better results.

The associate editor coordinating the review of this manuscript and approving it for publication was Amin Mahmoudi .

Transverse flux motors with coils wound around teeth are known to eliminate end-winding, have higher torque density, and better efficiency over conventional motors [5]. With separated, independent, and simple phase coils, they have a fault-tolerant advantage. Transverse flux motor's fundamental configuration is a U-shape array cores stator and two pole arrays rotor surrounding each phase coil [6], [7], [8], [9]. Even with the skewed option [6], reducing or eliminating cogging torque is still very challenging for the transverse flux motor. Moreover, in some cases, it is not even possible to apply skewing on the stator or rotor [10]. Meanwhile, compared to conventional machines, transverse flux machines suffer from low mechanical strength and high cost.

Axial flux motor topology is also a solution of potential end-winding removal. According to the analytical comparison studied in [11], axial flux motors have the advantages of high torque density, short overall length. Axial flux motors are always used in applications with limitations on axial lengths, such as wind energy systems, in-wheel motors, and aerospace applications [12], [13]. Detailed characteristics and

designs of different types of axial flux motors are discussed in [14]. Despite the high torque density potential, axial flux motors still face challenges in terms of mechanical manufacturing and thermal management capabilities.

The axial-radial hybrid flux machine is a novel machine type that incorporates both axial flux magnetic circuit and radial flux magnetic characteristics to enhance space utilization of winding and therefore improve torque density [15]. The axial stator with a complex 3D structure is made of solid material instead of lamination with iron loss considerations. Using a similar stator geometry, the innovative fan-ring shaped windings successfully integrate fan-shaped and ring-shaped winding designs [16], leading to reduced end-winding length. However, this advancement poses challenges in the production of pre-formed coils. In [17] and [18], two distinct types of axial-radial flux machines have demonstrated novel designs focusing on the rotor flux path instead of the stator, both exhibiting significant improvements in output torque performance.

A type of Dual-Rotor Modular-Stator Hybrid-Excited Axial-Flux Permanent Magnet Vernier Machine are introduced in literature [19]. This novel machine utilizes a modular stator and consequent-pole PM rotor to achieve adjustable air-gap flux densities, resulting in improved torque density and flux-weakening capability. The study discusses design considerations, operation principles, and air-gap flux density distributions. Through 3-D finite-element analysis, it is shown that a pole ratio of 8/1 offers higher torque density, machine efficiency, and flux-weakening capability compared to other ratios.

Hybrid excitation motors, which integrate permanent magnet and field winding excitation techniques, are discussed in the paper [20]. Three categorization approaches, including reluctance circuit, excitation system location, and geometrical placement of excitation, are explored. These motor configurations offer advantages such as independent control, enhanced power density, torque capability, and efficiency. The study encompasses design considerations, optimization techniques, and implementation challenges, providing a foundation for further research on the benefits and advancements of hybrid flux electrical machines. The paper [21] introduces a novel type of radial hybrid flux motor topology, referred to as the "Novel Dual-Stator Synchronous Machine with Permanent Magnet-Reluctance Composite Rotor." This specific motor configuration has been demonstrated to possess a higher capability for producing torque. Furthermore, it shows a novel way of integrating two rotors in one shaft with magnetic isolation in consideration.

Basing on the above research, this paper proposes a novel End-Winding Flux Machine (EHFM) consisting of an L-shape radial-axial flux stator and an axial-flux disk-shaped rotor in Section II. Without changing the conventional radial flux motors winding, but also improve the thermal capability of end-winding, a so called End-Winding Machine (EWM) is designed to be embedded in a conventional radial flux motor's end-winding and operate with the main motor synchronously

without causing any winding extension, hence form the EHFM. To synchronize with the main motor for the same winding length, EHFM shares the same slot/pole combination as the main motor. The disk-shaped rotor and main rotor are connected to the same shaft. To keep the iron loss low and magnetic capability high, conventional lamination with glue is used for teeth. The EHFM with L-shape teeth is analyzed and optimized using 3D Finite Element Method (FEM) in Sections III and IV. The results are experimentally validated in Section V. Finally, Section VI draws a conclusion for the research.

II. END-WINDING FLUX MOTOR
In this section, the concept of EHFM is clarified, which is implemented based on a conventional interior permanent magnet motor, i.e., #M1. The #M1 is first introduced as the benchmark design, followed by the concept description of EHFM.

A. BENCHMARK MOTOR: # M1
A 36-slot 8-pole motor with distributed winding and an interior V-shape permanent magnet configuration is employed as the benchmark motor, as depicted in Fig. 1. This motor represents the third-generation optimized design within our research group, intended for small electric vans. Our prior research in this domain yielded results that align with the conclusions presented in [23], which supports the advantages of the single V-shape magnet configuration. The specifications of the benchmark motor are listed in Table 1. The rated speed is 2800 rpm and rated torque is 120 Nm.
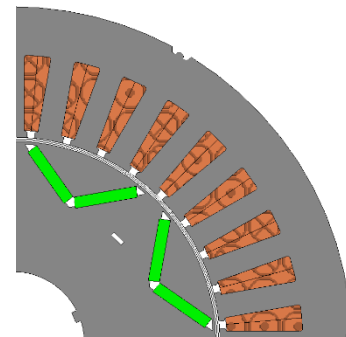

FIGURE 1. Design geometry of #M1.

B. CONCEPT DESCRIPTION OF EHFM
The pros and cons of distributed winding and concentrated winding have been compared in many cases [22]. Unlike concentrated winding, distributed winding requires a longer distance throughout the slots for the winding pitch, which results in a larger end-winding interspace, as presented in Fig. 2. The design of EHFM aims to utilize the interspace area between end windings by incorporating an EWM (End-Winding Machine).

The concept of EHFM is shown in Fig. 3, where the EWM is embedded into the original radial flux machine #M1,

TABLE 1. #M1 Design parameters.

Parameters	Value
Stator outer/Inner diameter	122.5/75 mm
Rotor outer/Inner diameter	73.5/42.4 mm
Active length	120 mm
Number of poles (p)	8
Slot number/Layers per slot	36/2
Active length	120 mm
End winding axial length top/bottom	25/45
Rated speed	2800 rpm
Rated torque	120 N·m
Teeth flux density	1.73 T
Advanced torque angle	20º
Rotor skewing angle	10º

FIGURE 2. End-winding interspace of #M1.

(a)

(b)

FIGURE 3. Proposed structure for EHFM. (a) EHFM cross section. (b) 3D plot: 1-disk rotor yoke. 2-Disk rotor magnet. 3-Sharing coils. 4-L-shape teeth. 5-Ring rotor. 6-#M1 (benchmark motor).
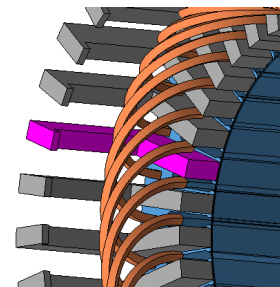
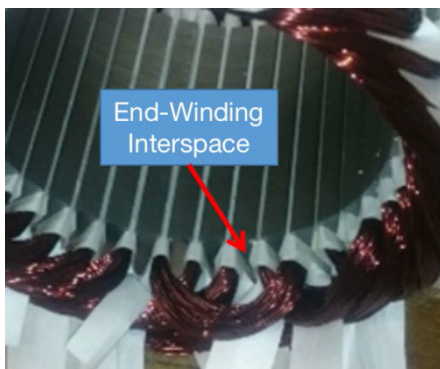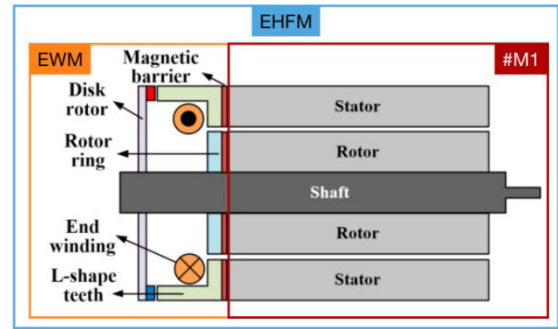FIGURE 4. Pink-L-shape teeth, Orange-end-winding, Blue-#M1 stator.

FIGURE 5. Concept of the flux path of EWM.

sharing armature winding and shaft. The slot-pole combination of EWM remains the same as #M1, allowing the induced flux from EWM and #M1 to be coupled. The stator module of the EWM consists of 4 L-shaped teeth and 3 sharing coils (end-winding), as shown in Fig. 3. As depicted in Fig. 4, an L-shaped laminated tooth can be placed in each interspace, forming the stator array altogether. The EWM rotor module is composed of 1 disk rotor yoke, 2 disk rotor magnets, and 5 ring rotor. Furthermore, magnets (inner or outer ring) are placed on the disk rotor to close the flux loop on the rotor side and generate the flux. Every 4 L-shape teeth of EWM is aligned with 6 stator teeth of #M1, while all the rotors are mechanically connected with a single shaft, thus guaranteeing synchronous operation with the same armature winding.
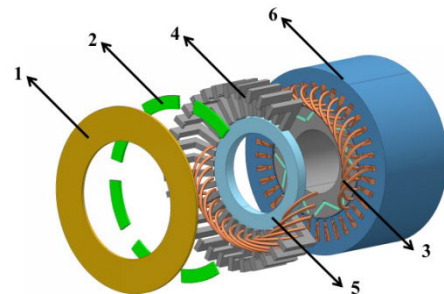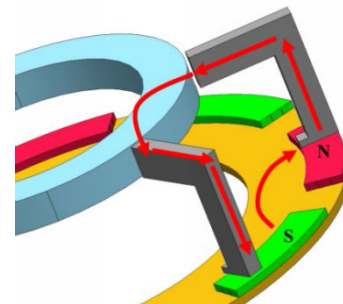
The operating principle of the EWM can be explained with the no-load magnetic path in Fig. 5. The magnetic flux generated by the disk rotor's north-pole crosses the disk-shaped air-gap into the L-shape teeth and then reaches the laminated ring-rotor through the ring air-gap. The return flux follows a symmetrical path and eventually returns to the south-pole. On the disk rotor in Fig. 5, the magnetic flux inside the solid iron disk connects the flux between the adjacent north/south-poles.

III. ANALYTICAL VALIDATION OF EWM

To validate the theoretical concept of EWM, this section establishes a simplified model in Fig. 6 and an equivalent

magnetic circuit diagram, in Fig. 7, for analytical validation. The magnetic structure network of a pole pitch for EWM is depicted in Fig 6. For the equivalent magnet circuit of EWM, the assumption of infinite iron permeability is made for the idealization model.
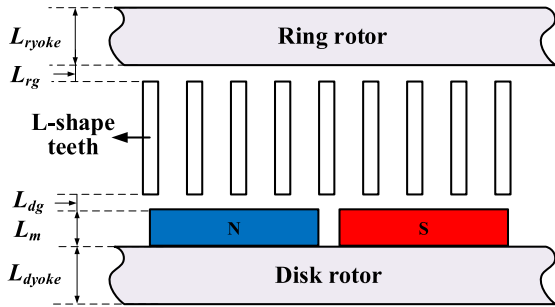
FIGURE 6. Concept of EWM axial cross section.

(a)

(b)

FIGURE 7. Equivalent magnetic circuit for single teeth.

In EWM, due to the relatively small permeability of air, there is a noticeable amount of MMF drop when crossing the air-gap, which emphasizes the importance of the air-gap for calculations of the equivalent magnetic circuit. Building upon the theoretical framework for fringing flux leakage calculation method introduced in [4] and incorporating the simplified formula, the air-gap flux density is calculated under the assumption that the air-gap flux path between the stator and rotor is equivalent, whereas the conventional motor has a comparatively small slot-opening. EWM slot-opening is wide. As teeth width (W_{teeth}) is small, the extension flux path at the edge of the teeth creates a fringing area (L_{ex1}, L_{ex2} in Fig. 8). As the teeth/slot-opening ratio is high in EWM, the fringing area in EWM is significant and therefore should be considered. Moreover, the different diameters between the inner side-teeth and outer-side teeth are causing variance in the inner and outer slot-opening. Hence, a more accurate estimation of 'equivalent air-gap length' L_{gave}, called an average air-gap method (AAM), is presented below in equation (1), where 'L_g' refers to air-gap length and 'L_{ex}' is fringing area.

$$L_{gave} \approx \frac{\left(\frac{2\pi L_{ex}}{4} + L_g\right) \cdot L_{ex} + W_{teeth}L_g}{W_{teeth} + 2L_{ex}} \quad (1)$$

The average air-gap length is the average height of the air-gap flux path area. The width of the air-gap is presented as the denominator of the equation, which is the PM effective length of each tooth (pole-arc). The air-gap flux path area is assumed to be the sum of the two 'distortion arc areas' and one 'rectangular area', where the distortion arc is approximated as a quarter of a circular. For this reason, with the 'equivalent air-gap length', the calculation of air-gap reluctance can be made as follows:

$$\Phi_{g1} = \Phi_r \times \frac{R_{leak1}}{\left[R_{g1} + \frac{R_{g2}R_{leak2}}{R_{g2}+R_{leak2}}\right] + R_{leak1}} \quad (2)$$

$$\Phi_{g2} = \Phi_{g1} \times \frac{R_{leak2}}{R_{g2} + R_{leak2}}$$

$$B_{g1} = \frac{\Phi_{g1}}{A_{g1}}$$

$$B_{g2} = \frac{\Phi_{g2}}{A_{g2}} \quad (3)$$

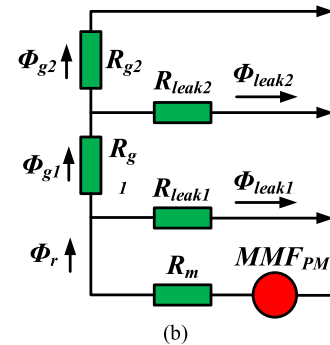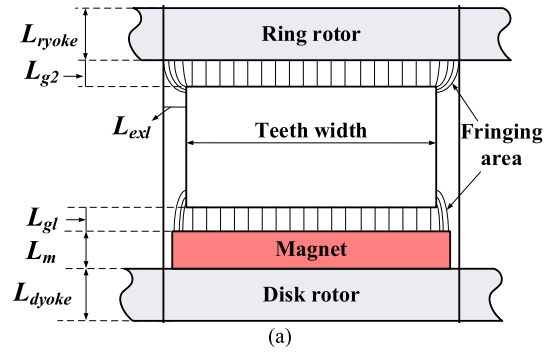In equation (2), leakage reluctance R_{leak1} and R_{leak2} are all assumed to be $R_{leak1} = R_{leak2} = R_m$.

The total leakage factor f_{LKG} of the axial flux machine consists of axial leakage $f_{leak-axial}$ and radial leakage $f_{leak-radial}$. This approach is called the 'leakage flux method' and can predict the f_{LKG} with the following equation:

$$f_{LKG} = \frac{1}{\frac{1}{f_{leak-axial}} + \frac{1}{f_{leak-radial}} - 1} \quad (4)$$

With $L_g = 1.5$ mm, $L_m/L_g = 3.3$, and $\alpha_p = 0.7$, $f_{leak-axial}$ range is given as 0.75~0.8 and $f_{leak-radial}$ range is provided as 0.75~0.9.

$$\Phi_{g1} = \Phi_r \times f_{LKG1}$$
$$\Phi_{g2} = \Phi_{g1} \times f_{LKG2} \quad (5)$$

EWM is regarded as a disk motor combined with a radial flux motor (RING rotor). For air-gap 1 on the disk rotor, f_{LKG1} is calculated as 0.60 ($f_{leak-axial} = 0.75$ and $f_{leak-radial} = 0.75$). Since the inner stator has larger and unevenly distributed air-gap compared to the conventional motor, its leakage factor f_{LKG1} is estimated at 0.7, $B_{g1} = 0.73$T and $B_{g2} = 0.51$T. Based on the derived analytical formulas from the previous section, the feasibility of the EWM design principle has been demonstrated. However, due to the complexity of the motor structure, which differs from traditional motors, the simplified model cannot accurately calculate the motor parameters. Therefore, the next section will focus on modeling and conducting a more in-depth analysis using 3D finite element methods.

IV. EHFM 3D FEM ANALYSIS

The analytical approach for evaluating the performance of EHFM is challenging, especially when #M1 and EWM are combined. Therefore, in this section, a 3-D FEM modeling approach is used for further performance study.

A. 3D MODELING OF EHFM INITIAL DESIGN

In Fig. 8, three 3D FEM models, (a) #M1, (b) EWM and (c) EHFM, are built in the software of Infolytica MagNet for further validation and design optimizations.

To firstly validate the concept design of EWM in section II and analytical concept in section III, in Fig. 9, a 3D simulation model of the EWM under no-load conditions is established. The simulation results provide evidence that supports the proposed flux path concept presented in Fig. 5.
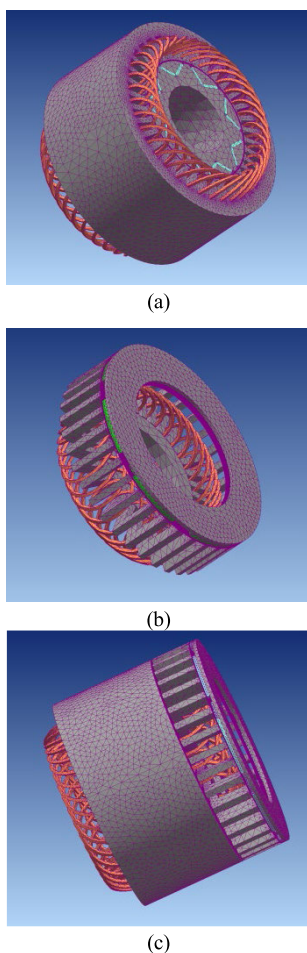

(a)

(b)

(c)

FIGURE 8. FEM 3D models with mesh: (a) #M1. (b) EWM. (c) EHFM.

TABLE 2. #M1 and EHFM FEM results-1 initial design.

Motor	#M1 (3D)	EWM (3D)	EHFM (3D)
Torque (Nm)	120.3	10.5	129.3

In Table 2, a further comparison of the loaded condition is presented for the three machines: #M1, EWM, and EHFM, under the rated current of 120A. Firstly, the simulation results
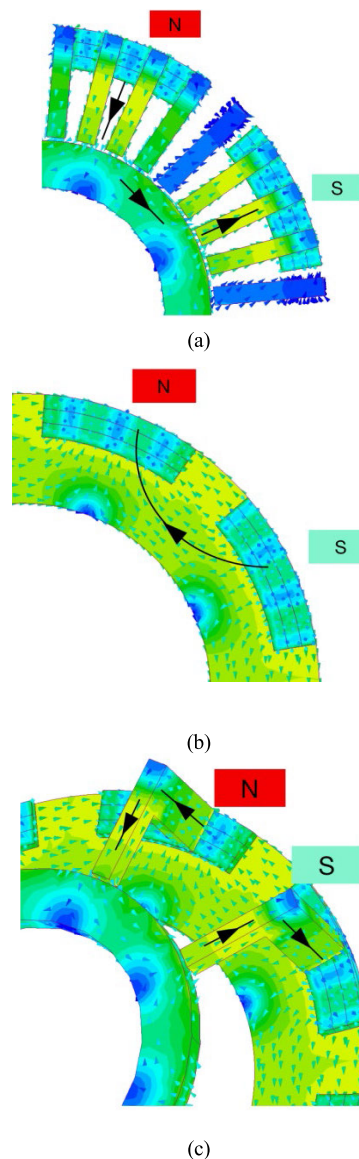

(a)

(b)

(c)

FIGURE 9. No-load magnetic flux path for the EWM: (a) Stator and ring-rotor. (b) Rotor. (c) L-shape teeth.

for EWM validate the feasibility of the design. However, there is a deviation from the design theory as the torque generated by EHFM does not reach the expected sum of #M1 and EWM. Therefore, in subsequent research, an analysis of this phenomenon will be conducted, followed by optimization efforts to address this discrepancy.

B. OPTIMIZATION OF 3D FLUX PATH ON FLUX LEAKAGE

To investigate the results in table 2, The contact region of EHFM between EWM and #M1 is investigated, in terms of flux leakage and magnetic short-circuit. The changing magnetic reluctance in the contact region creates unexpected flux path, requiring careful observation of the electromagnetic behavior. To investigate the flux leakage, several no-load 3D FEM models are built. In order to study the flux leakage

from #M1 to EWM, the disk rotor magnet has been set into de-magnetized mode. The shaded plot of both stator and rotor modules are shown in Fig. 10 and Fig. 11.

(a)

(b)

(c)
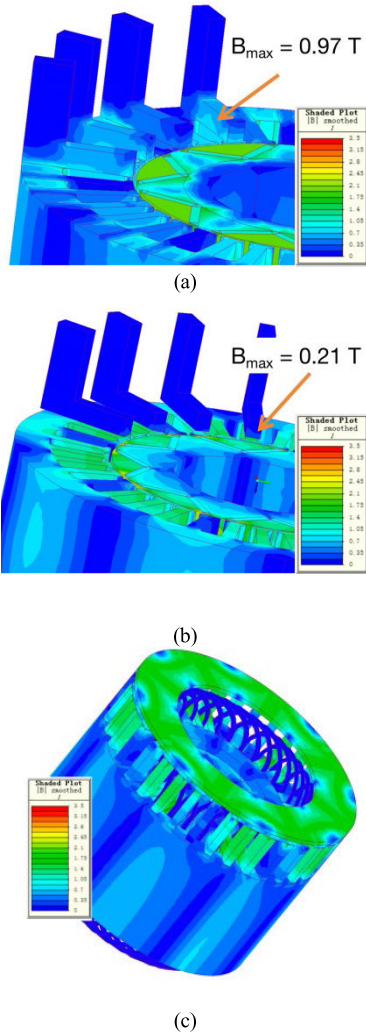
FIGURE 10. EHFM 3D FEM results disk rotor de-magnetized (a) without magnetic barrier (b) with 2 mm magnetic barrier (c) EHFM full model with 2 mm magnetic barrier.

The Fig. 10 studies the flux leakage on EHFM stator part, between EWM L-shape tooth and #M1 stator. Without magnetic barrier layer in (a), some parts of the flux generated from #M1 rotor magnets leaks into the L-shape tooth and hence caused stator leakage. By setting a 2 mm magnetic barrier distance in between (b), the stator leakage phenomenon can be fully optimized. With disk rotor magnetic active, the EHFM full model with 2 mm magnetic barrier in Fig. 10 (c) is also showing that the flux leakage has been reduced into very low level.

In Fig. 11(a), it can be observed that the direct contact area between the ring rotor and #M1 rotor creates a path of lower reluctance across the airgap. This leads to a notable magnetic "short-circuit" between the two rotors, resulting in a decrease in torque for EHFM as indicated in table 2.
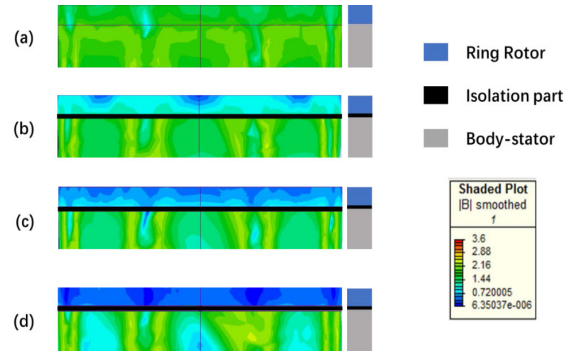
FIGURE 11. EHFM rotor magnetic barrier: (a) no magnetic barrier. (b) 1 mm magnetic barrier. (c) 1.5 mm magnetic barrier. (d) 2 mm magnetic barrier.

On the EHFM stator side, the magnetic barrier gap length of 2 mm has already demonstrated effective suppression of leakage, as shown in Fig. 10(b). In Fig. 11, the length of the magnetic barrier layer is further investigated to determine its impact on the magnetic "short-circuit" phenomenon. The findings reveal that when the magnetic barrier layer length matches the #M1 air-gap, namely 1.5mm, the occurrence of the "short-circuit" is significantly diminished. Moreover, in Fig. 11(d), with the barrier length of 2 mm, the magnetic short-circuit has been successfully suppressed. As anticipated, the inclusion of the magnetic barrier in the FEM analysis has resulted in improvements in the EHFM torque, as demonstrated by the results in Table 3 compared to Table 2.

TABLE 3. #M1 and EHFM FEM results-2 refined design with magnetic isolation.

Motor	#M1 (3D)	EWM (3D)	EHFM (3D)
Torque (Nm)	120.3	10.5	130.8

### C. OPTIMIZATION OF EWM TORQUE PERFORMANCE

To further investigate the torque performance of the End-Winding Flux Machine (EWM), the optimization of the L-shape teeth and magnet step skewing has been studied as shown in Fig. 12.

In accordance with the EWM concept, the selection of conventional lamination sheets for the L-shape teeth was based on their advantageous characteristics, including a lower iron loss coefficient, higher B-H capability, and cost-effectiveness. However, due to the specific design of the L-shape teeth, they can only be laminated with L-shape sheets, which restricts the cross-section shape to a rectangular form, as depicted in Fig. 12 (a) and Fig. 16 (a). This limitation is further compounded by the presence of the liner and magnetic barrier under the end-winding coil in Fig. 4 (pink) and Fig. 12 (a) (light gray), thus limiting the total cross-sectional area of the L-shape teeth.

In the EWM motor, a higher cogging torque is induced, which affects torque ripple due to the arrangement of the L-shape teeth array resulting in a parallel teeth structure,

as observed in Fig. 12 (a) and Fig. 4. The width of the L-shape teeth is significantly smaller compared to #M1, resulting in a relatively larger slot opening. This phenomenon is more pronounced at the disk rotor end. Since applying stator skewing to the laminated L-shape teeth is mechanically challenging, an alternative approach is considered: skewing the magnets, as illustrated in Fig. 12 (b).
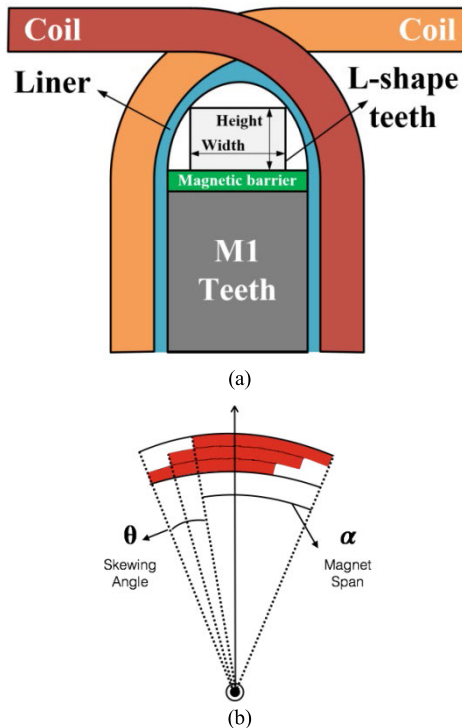
FIGURE 12. (a) Crossing area of the L-shape end-teeth. 1—Middle End-teeth height. 2—Middle End-teeth width. (b) Magnet step skew.

Considering the changes in height as shown in Fig. 12 (a) and the magnet step skew illustrated in Fig. 12 (b), the results have been compared in Fig. 13. In order to fully utilize the available space in a half-circle shape with a rectangular configuration, any alterations in the height of the L-shape teeth structure will directly influence the width, consequently impacting the total cross-sectional area of the teeth, as depicted in the gray curve in Fig. 13 (a). The results indicate that with a teeth height of 15mm, both the cross-sectional area (gray) and the average torque (blue) reach their maximum values. Furthermore, with the optimal teeth height of 15mm, the torque performance before and after magnet step skew has been compared in Fig. 13 (b) and (c). It is evident that the cogging torque of the EWM has been reduced from 3.7 Nm to 0.9 Nm, and the torque ripple has decreased from 18.5% to 2.5%.

The further investigation into the 3D modeling comparison between #M1 and the End-Winding Hybrid Flux Machine (EHFM) has been conducted. The torque-speed curve is examined in Fig. 14 (a). In this analysis, a current of 120A is limited by a DC voltage cap of 400V. The results
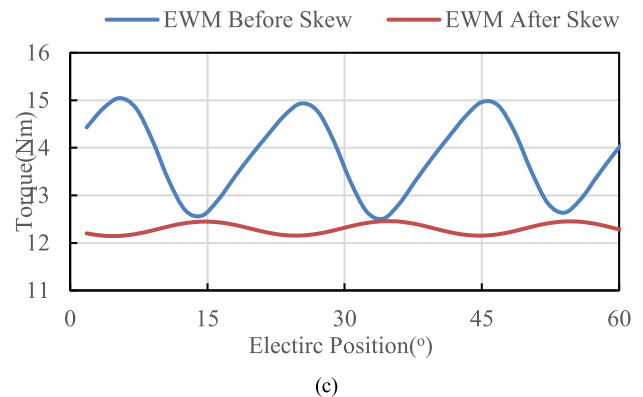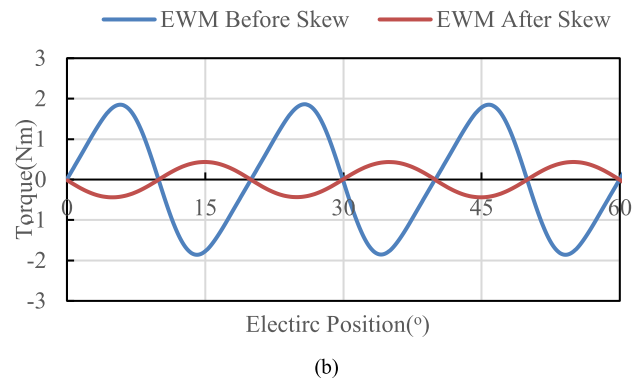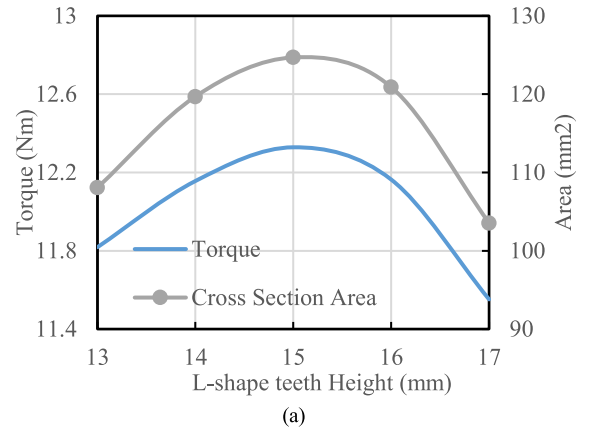
FIGURE 13. EWM 3D FEM results of (a) L-shape teeth height vs. Average torque after skew and cross-sectional area. (b) EWM torque ripple before vs. after skew with 15mm teeth height. (c) EWM cogging before vs. after skew with 15mm teeth height.

highlight EHFM's superior performance in terms of maximum torque when compared to #M1. Moreover, due to the higher back-EMF generated in EHFM, the field weakening point initiates earlier than in #M1. Nevertheless, EHFM's flux weakening capability is comparatively weaker, attributed to the absence of rotor saliency in the disk rotor design.

In Fig. 14 (b) and (c), the comparison between EHFM and #M1 reveals that EHFM has a lower cogging torque of 3.0 Nm compared to #M1's 3.3 Nm and lower torque ripple of 1.7% compared to 1.9%. This is because the cogging torque waveform of #M1 has been compensated by the waveform of the EWM.
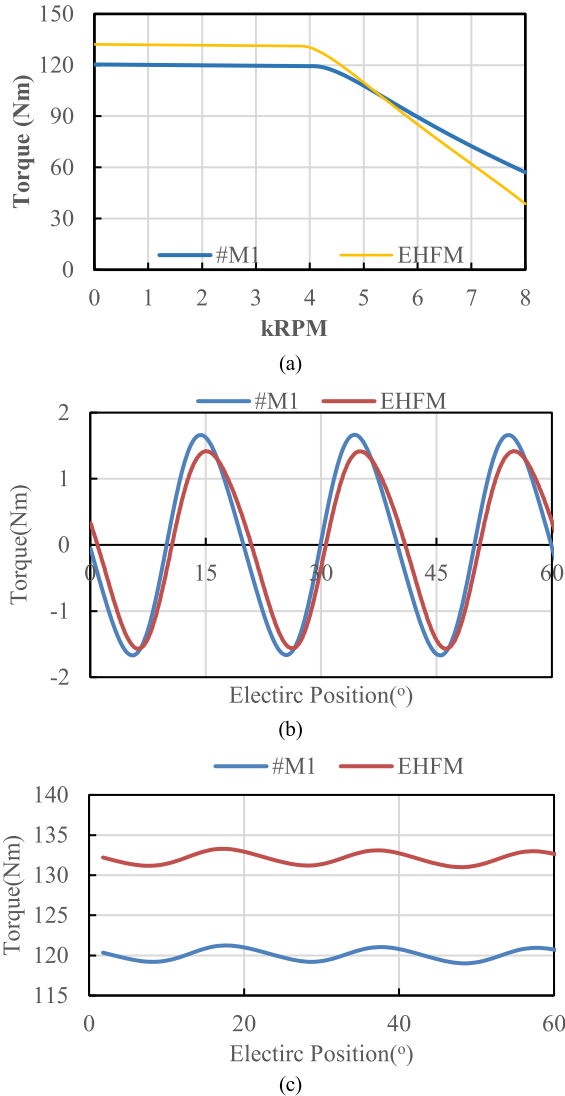
FIGURE 14. 3D FEM results of #M1 vs EHFM (a)Torque-speed curve with 120A under 400V. (b) Cogging torque waveform. (c) Torque ripple.

TABLE 4. #M1 and EHFM FEM results-3 Optimized design.

Motor	#M1 (3D)	EWM (3D)	EHFM (3D)
Torque (Nm)	120.3	12.3	132.1

This particular height yields a maximum average torque of 12.3 Nm. The optimized design, as presented in Table 4, demonstrates improved torque performance for both EWM and EHFM compared to Table 3. It is noteworthy that these improvements are achieved without altering the overall dimensions of the EHFM.

V. EXPERIMENTAL VALIDATION

To validate all the design aspects discussed earlier, including the analytical and FEM analyses that demonstrated the design concept and torque performance optimization of EHFM, the proposed EHFM is manufactured and subjected to experimental testing in this section. This validation process aims to provide empirical evidence and ensure the practical applicability of the EHFM design.
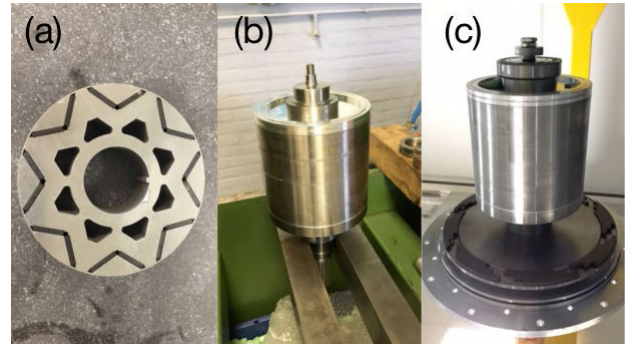

FIGURE 15. Prototype rotor parts. (a) Radial-flux rotor for both #M1 and EHFM. (b) #M1 rotor. (c) EHFM rotor.

Since #M1 and EWM share the same active parts of radial flux rotor, the manufacturing of EWM rotor only requires a simply change of rotor shaft and placing the EHFM rotor, as shown in Fig. 15. In Fig. 16, EWM stator is first assembled with laminated L-shape teeth, isolation layer, and #M1 stator, before winding. The magnetic barrier layer is designed not only to create magnetic barrier distance between two stators but also to position the 36 pieces of L-shape teeth.
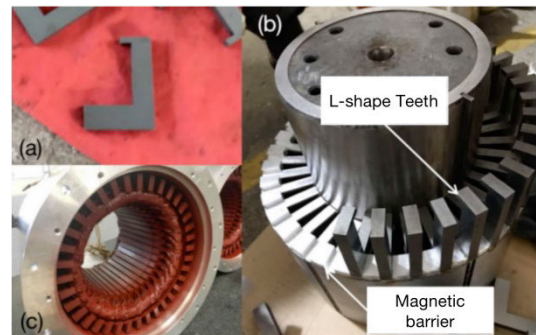

FIGURE 16. EWM prototype stator parts. (a) L-shape teeth. (b) Stator assembly with #M1 stator, magnetic barrier layer, and L-shape teeth. (c) Stator ready for assembling.

Motor test-rig in Fig. 17 is set up for the experimental validation. Fig. 18 shows the comparisons of line-line back-EMF between #M1 and EHFM at 2800 rpm. It can be seen that the experimental results agree well with the FEM results, with small deviations, where the error on #M1 and EHFM are 4% and 3%, due to (i) inaccurate stacking factor in the manufacturing process, (ii) measurement error, and (iii) partial and theoretical material parameter difference.

To further validate the rated point performance, both the original motor, referred to as motor #M1, and the proposed motor EHFM, were operated in the rotating mode for on load tests. As shown in TABLE 5, the rated performance and static parameters are listed for both #M1 and EHFM. The measured line-line resistances for both #M1 and EHFM are identical, confirming that the two motors have the same length
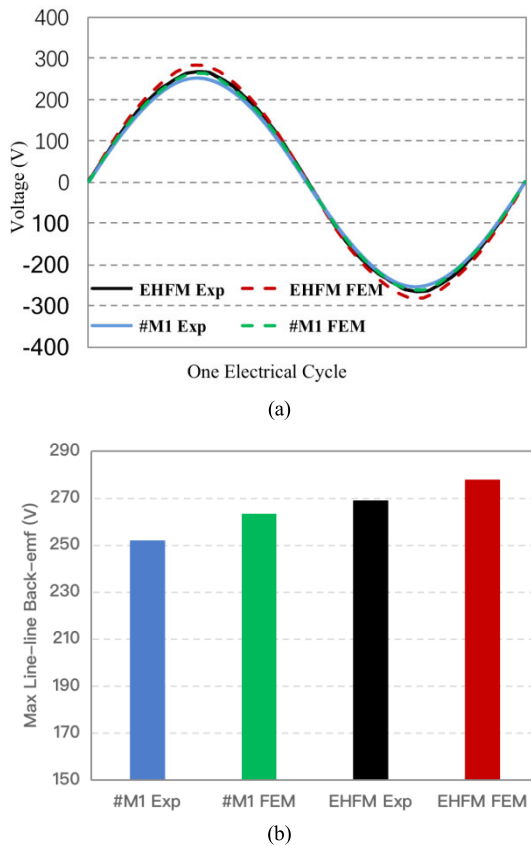
FIGURE 17. EHFM on Test-rig.

(a)

(b)

FIGURE 18. Line-line Back-EMF results comparison. (a) waveform. (b) amplitude in maximum.

TABLE 5. #M1 and EHFM Experimental Data @2800 rpm.

Parameters	#M1	EHFM
Line current	119.9 A	120.2 A
Average Torque	120 Nm	131 Nm
Torque per amp	1.01 Nm/A	1.09 Nm/A
Torque per active Volume	11.6 kNm/m3	12.0 kNm/m3
Torque per active weight	2.2 Nm/kg	2.1 Nm/kg
L-L Resistance	32 m Ω	32 m Ω
Power Factor	0.89	0.92
No-load losses	0.5 kW	1.0 kW
On-load losses	1.8 kW	2.2 kW
Efficiency	94.8%	94.2%
Output power	35.2 kW	38.4 kW
End-Winding Temperature	63ºC	56ºC
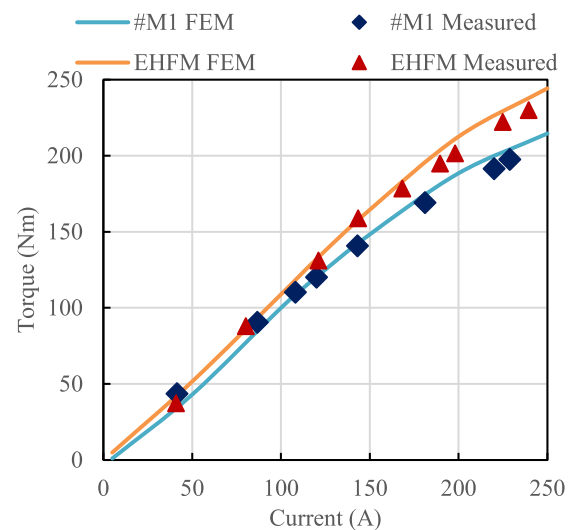
FIGURE 19. Comparison of dynamic torque obtained from FEM and measurement.

of the armature winding. Moreover, the results rated measured results demonstrate that the EHFM exhibits improved torque performance compared to the conventional benchmark motor #M1. This improvement is evident in terms of average torque, torque per amp, and torque-to-volume density. During the rated test, the end-winding temperature has been captured from the thermal couple in the same position on the end-winding of both motor. The result of EHFM (56ºC) was showing 7ºC thermal improvement over #M1 (63ºC), which proves the theory that the structure of the EWM would improve the motor end-winding temperature.

Further more, the torque capability of both motor has been measured and compared with FEM results in Fig. 19, where the motor was set to 1000 rpm and the line current was injected from 0 to 240 A. The results show that the experimental results of torque for both #M1 and EHFM are aligning well with the FEM data, especially within the rated current region of 120 A. The improvement is evident in terms of average torque, torque per amp, and torque-to-volume density. However, the torque-to-weight density of the EHFM prototype is lower since it does not consider any weight reduction measures on the active parts. Further weight reduction can be explored, considering both electromagnetic and mechanical designs, focusing on disk-rotor weight reduction, L-shape teeth optimization, and ring-rotor weight reduction.

VI. CONCLUSION

In conclusion, the proposed EWM technique effectively mitigates the end-winding effects by combining with the

benchmark motor #M1 to form the EHFM system. This combined system is synchronized both electrically and mechanically, as the main body #M1 and EHFM use the same slot/pole combinations. Analytical and 3D FEM models were used to analyze the system performance, and optimization was performed to maximize the average torque output, reduce torque ripple and cogging torque by implementing an optimized L-shape teeth dimension and appropriate skewing of the magnet shape. The experimental results of the prototype show a notable 9.2% increase in torque and 7 °C end-winding thermal reduction, compared to the original motor design. The EHFM has great potential in various applications where high torque output and low cogging torque are essential. Further investigations are warranted to explore areas such as weight reduction, leakage reduction, iron loss reduction, manufacturing process optimization, cost reduction and other related aspects. These avenues of research hold promising potential for optimizing EHFM systems, enhancing their efficiency, and opening up new possibilities for various applications in the field.

REFERENCES

[1] K. Takeuchi, M. Matsushita, H. Makino, Y. Tsuboi, and N. Amemiya, "Finite-element analysis for magnetic flux in end region of synchronous machine using end-winding model," *IEEE Trans. Magn.*, vol. 57, no. 2, pp. 1–6, Feb. 2021.

[2] Y. Yao, H. Xia, G. Ni, X. Liang, S. Yang, and P. Ni, "3-D eddy current analysis in the end region of a turbogenerator by using reduced magnetic vector potential," *IEEE Trans. Magn.*, vol. 42, no. 4, pp. 1323–1326, Apr. 2006.

[3] D. Lin, P. Zhou, Y. Hu, and M. Rosu, "Analytical computation of end-winding leakage inductance for multi-phase AC machines," in *Proc. IEEE Int. Electr. Mach. Drives Conf. (IEMDC)*, May 2017, pp. 1–6.

[4] G. Kostro, M. Michna, F. Kutt, and R. Ryndzionek, "Improved methods for stator end winding leakage inductance calculation," *COMPEL Int. J. Comput. Math. Electr. Electron. Eng.*, vol. 42, no. 4, pp. 972–980, Jun. 2023.

[5] J. G. Zhu, Y. G. Guo, Z. W. Lin, Y. J. Li, and Y. K. Huang, "Development of PM transverse flux motors with soft magnetic composite cores," *IEEE Trans. Magn.*, vol. 47, no. 10, pp. 4376–4383, Oct. 2011.

[6] Y. Ueda, H. Takahashi, A. Ogawa, T. Akiba, and M. Yoshida, "Cogging-torque reduction of transverse-flux motor by skewing stator poles," *IEEE Trans. Magn.*, vol. 52, no. 7, pp. 1–4, Jul. 2016.

[7] M. F. J. Kremers, J. J. H. Paulides, and E. A. Lomonova, "Toward accurate design of a transverse flux machine using an analytical 3-D magnetic charge model," *IEEE Trans. Magn.*, vol. 51, no. 11, pp. 1–4, Nov. 2015.

[8] J. H. Chang, J. Y. Lee, J. W. Kim, and S. U. Chung, "Inner rotor type permanent magnet excited transverse flux motor," U.S. Patent 7 952 252, May 31, 2011.

[9] A. Hirzel, "Radial airgap, transverse flux motor," U.S. Patent 10 864 041, Dec. 16, 2004.

[10] O. Dobzhanskyi and R. Gouws, "Performance analysis of a permanent magnet transverse flux generator with double coil," *IEEE Trans. Magn.*, vol. 52, no. 1, pp. 1–11, Jan. 2016.

[11] J. R. Hendershot and T. J. E. Miller, *Design of Brushless Permanent-Magnet Machines*. Venice, FL, USA: Motor Design Books, 2010.

[12] S. Amin, S. Khan, and S. S. Hussain Bukhari, "A comprehensive review on axial flux machines and its applications," in *Proc. 2nd Int. Conf. Comput., Math. Eng. Technol. (iCoMET)*, Jan. 2019, pp. 1–7.

[13] B. Zhang, T. Seidler, R. Dierken, and M. Doppelbauer, "Development of a yokeless and segmented armature axial flux machine," *IEEE Trans. Ind. Electron.*, vol. 63, no. 4, pp. 2062–2071, Apr. 2016.

[14] J. F. Gieras, R.-J. Wang, and M. J. Kamper, *Axial Flux Permanent Magnet Brushless Machines*. Cham, Switzerland: Springer, 2008.

[15] S. S. Nair, N. Shamsuddeen, and S. J. Dhinagar, "A novel electromagnetic core structure for axial radial flux permanent magnet electric motor," in *Proc. 6th IET Int. Conf. Power Electron., Mach. Drives (PEMD)*, Mar. 2012, pp. 1–6.

[16] X. Wei, K. Yang, Z. Pan, H. Xie, C. Zhu, and Y. Zhang, "Design of a novel axial-radial flux permanent magnet motor," in *Proc. 17th Int. Conf. Electr. Mach. Syst. (ICEMS)*, Oct. 2014, pp. 80–84.

[17] W. Yan, W. Wang, H. Li, H. Chen, F. Yu, D. Zhang, and H. Yang, "Performance analysis of a novel axial radial flux segmental rotor switched reluctance motor," *IEEE Trans. Transport. Electrific.*, early access, May 2, 2023, doi: 10.1109/TTE.2023.3272402.

[18] L. Li, J. Cao, B. Kou, S. Yang, D. Pan, and H. Zhu, "Design of axial and radial flux HTS permanent magnet synchronous Motor's rotor," *IEEE Trans. Appl. Supercond.*, vol. 20, no. 3, pp. 1060–1062, Jun. 2010.

[19] L. Jia, M. Lin, K. Lin, W. Le, and A. Yang, "Design and analysis of dual-rotor modular-stator hybrid-excited axial-flux permanent magnet Vernier machine," *Energies*, vol. 15, no. 4, p. 1458, Feb. 2022.

[20] G. Mörée and M. Leijon, "Overview of hybrid excitation in electrical machines," *Energies*, vol. 15, no. 19, p. 7254, Oct. 2022.

[21] Y. Zhang, S. Yu, G. Liu, and H. Zhang, "Comparative research for a novel dual-stator synchronous machine with permanent magnet-reluctance composite rotor," *IEEE Trans. Appl. Supercond.*, vol. 30, no. 4, pp. 1–5, Jun. 2020.

[22] H. Zhao, X. Zhang, J. Li, L. Xu, S. Wang, and H. Zhang, "An advanced propulsion motor with enhanced winding cooling system for a solar-powered aircraft," *IEEE Trans. Transport. Electrific.*, early access, Jun. 13, 2023, doi: 10.1109/TTE.2023.3285608.

[23] Y. Yang, S. M. Castano, R. Yang, M. Kasprzak, B. Bilgin, A. Sathyan, H. Dadkhah, and A. Emadi, "Design and comparison of interior permanent magnet motor topologies for traction applications," *IEEE Trans. Transport. Electrific.*, vol. 3, no. 1, pp. 86–97, Mar. 2017, doi: 10.1109/TTE.2016.2614972.

BOWEN SHI was born in Hangzhou, China, in 1990. He received the B.S. and Ph.D. degrees in electrical engineering from the University of Nottingham, Nottingham, U.K., in 2013 and 2018, respectively.

He is currently a Senior Engineer with the Nottingham Electrification Center, University of Nottingham, and a Postdoctoral Researcher with the College of Electrical Engineering, Zhejiang University, Hangzhou. His main research interest includes PMSM design for traction applications.

XIAOYAN HUANG (Member, IEEE) received the B.E. degree in control measurement techniques and instrumentation from Zhejiang University, Hangzhou, China, in 2003, and the Ph.D. degree in electrical machines and drives from the University of Nottingham, Nottingham, U.K., in 2008.

From 2008 to 2009, she was a Research Fellow with the University of Nottingham. Currently, she is a Professor with the College of Electrical Engineering, Zhejiang University, where she is working on electrical machines and drives. Her research interests include PM machines and drives for aerospace and traction applications and generator system for urban networks.

JING LI (Senior Member, IEEE) received the B.Eng. and M.Sc. degrees (Hons.) from the Beijing Institute of Technology, Beijing, China, in 1999 and 2002, respectively, and the Ph.D. degree from the University of Nottingham, Nottingham, U.K., in 2010, all in electrical and electronic engineering.

After graduation, she was a Research Fellow with the Power Electronics, Machine and Control Group, University of Nottingham. In 2016, she joined the University of Nottingham Ningbo China, Ningbo, China, as an Assistant Professor, where she is currently an Associate Professor with the Department of Electrical and Electronic Engineering. Her research interests include condition monitoring for motor drive systems and power distribution systems, advanced control, and design of motor drive systems.

HE ZHANG (Senior Member, IEEE) received the B.Eng. degree from Zhejiang University, Hangzhou, China, in 2002, and the M.Sc. and Ph.D. degrees in electrical machines from the University of Nottingham, Nottingham, U.K., in 2004 and 2009, respectively.

He was a Research Fellow with the University of Nottingham, where he was the Director of the BestMotion Technology Centre. He moved to the University of Nottingham Ningbo China, Ningbo, China, as Senior Research Fellow, in 2014, promoted to a Principal Research Fellow in 2016 and a Professor in 2020. He is currently the Director of the Power Electronics, Machines and Control Research Group, Nottingham Electrification Centre (NEC), University of Nottingham Ningbo China. His research interests include high-performance electric machines and drives for transport electrification.

HAN ZHAO was born in Heilongjiang, China. He received the B.Eng. and M.Eng. degrees in electrical engineering from the Harbin Institute of Technology, Harbin, China, in 2012 and 2014, respectively. He is currently pursuing the Ph.D. degree with the Key Laboratory of More Electric Aircraft Technology of Zhejiang Province, University of Nottingham Ningbo China, Ningbo, China.

His main research interest includes electromagnetic and thermal analysis on electrical machines for electric propulsion applications. He received the Best Presentation Prizes at ICIT 2022 and ITEC Asia–Pacific 2022. The major research findings during his Ph.D. study has been awarded First Prize in the Ningbo Innovation in Science and Technology Competition.

XIAOCHEN ZHANG (Member, IEEE) received the master's degree from the Harbin University of Science and Technology, Harbin, China, in 2006, and the Ph.D. degree from the Harbin Institute of Electrical Technology, Harbin, in 2012.

He is with the Yongjiang Laboratory, and the University of Nottingham Ningbo China, Ningbo, China. His research interests include research on electromagnetic and thermal analysis on electrical machine, especially in permanent magnetic machines and high-speed machines. He is a fellow of the Royal Aeronautical Society (FRAeS).

FENGYU ZHANG (Member, IEEE) received the B.E. degree in thermal engineering from the Huazhong University of Science and Technology, Wuhan, China, in 2014, and the Ph.D. degree in electrical machines from the University of Nottingham, Nottingham, U.K., in 2019.

She is currently a Senior Research Fellow in thermal management on electrical machines with the Power Electronics, Machines and Control (PEMC) Group, University of Nottingham. Her main research interests include high-performance motors for transport applications and their multi-domain optimization.

CHRIS GERADA (Senior Member, IEEE) received the Ph.D. degree in electrical machines from the University of Nottingham, Nottingham, U.K., in 2005. Subsequently, he was a Researcher with the University of Nottingham, on high-performance electrical drives and the design and modeling of electromagnetic actuators for aerospace applications. He was appointed as a Lecturer of electrical machines (2008), an Associate Professor (2011), and a Professor (2013) with the University of Nottingham. He is the past Chair of the IEEE IES Electrical Machines Committee. He serves as an Associate Editor for IEEE TRANSACTIONS ON INDUSTRY APPLICATIONS.

• • •